Unravelling the impact of Ta doping on the electronic and structural properties of titania: A combined theoretical and experimental approach

Vignesh Kumaravel [a,b 1*], Maria Barbara Maccioni [c1], Snehamol Mathew [a,b], Steven J. Hinder [d], John Bartlett [a,b], Michael Nolan [c*], Suresh C. Pillai [a,b*]

[a] *Nanotechnology and Bio-Engineering Research Group, Department of Environmental Science, Faculty of Science, Institute of Technology Sligo, Ash Lane, Sligo F91 YW50, Ireland.*

[b] *Centre for Precision Engineering, Materials and Manufacturing Research (PEM), Institute of Technology Sligo, Ash Lane, Sligo F91 YW50, Ireland.*

[c] *Tyndall National Institute, University College Cork, Lee Maltings, Dyke Parade, Cork T12 R5CP, Ireland.*

[d] *The Surface Analysis Laboratory, Faculty of Engineering and Physical Sciences, University of Surrey, Guildford, Surrey GU2 7XH, United Kingdom.*

[1] *These authors are equally contributed to this work.*

Corresponding Author E-mail: Kumaravel.Vignesh@itsligo.ie; michael.nolan@tyndall.ie; Pillai.Suresh@itsligo.ie

Abstract:

The introduction of new energy levels in the forbidden band through the doping of metal ions is an effective strategy to improve the thermal stability of TiO_2. In the present study, the impact of Ta doping on the anatase to rutile transition (ART), structural characteristics, anion and cation vacancy formation were investigated in detail using Density Functional Theory (DFT) and experimental characterisation including, X-ray diffraction (XRD), Raman, and X-ray photoelectron spectroscopy (XPS). The average crystallite size of TiO_2 decreases with an increase in the Ta concentration. At high temperatures, more oxygen atoms entered the crystal lattice and occupy the vacancies, leading to lattice expansion. Importantly, we find that Ta doping preserved the anatase content of TiO_2 up to annealing temperatures of 850 °C which allows anatase stability to be maintained at typical ceramic processing temperatures. The substitution of Ti^{4+} by the Ta^{5+} ions increased the electron concentration in the crystal lattice through formation of Ti^{3+} defect states. Raman studies revealed the formation of new Ta bonds *via* disturbing the Ti-O-Ti bonds in the crystal lattice. It is concluded that under the oxidising conditions, Ta^{5+} ions could be enhanced on Ta-TiO_2 surface due to the slow diffusion kinetics.

Keywords: Anatase; Defects; Dopant; Titanium dioxide; Oxygen vacancy

1. Introduction:

Titanium dioxide (TiO_2) nanoparticles have been widely used for energy production, wastewater treatment, cosmetics, optics, self-cleaning and bio-medical applications [1]. Among its significant crystalline features, the anatase phase of TiO_2 is preferred for use in antimicrobial coatings and hydrogen production due to its higher activity compared to rutile [2, 3]. The rutile phase of TiO_2 is preferred for optoelectronic applications [2, 4]. Anatase has a simple tetragonal Bravais lattice, whereas that of the rutile has a body centred lattice [5]. The degree of octahedra distortion of anatase with D_{2d} local symmetry is greater than that of the rutile with inversion C_{2h} symmetry [5]. The lifetime of electrons in the anatase phase is nearly 100 times higher than that of rutile phase. In particular, the electron diffusion length of anatase is around 100 times larger than rutile [6, 7]. The electron diffusion length of anatase is more than 10 μm whereas that of rutile is only 100 nm [6].

The activity of TiO_2 in its applications is determined by its surface and interface characteristics [8]. Materials composed of a mixture of both crystalline phases, but with a high anatase content can promote the activity of TiO_2 through enhanced charge carrier separation at the catalyst surface. The performance of materials with heterophase junctions (engineering of a perfect phase interface within the semiconductor) are superior to conventional heterojunction catalysts (fabrication of a heterojunction catalyst from two different semiconductors with respect to their band alignment) [9], which facilitates electron transfer [10]. In addition, the existence of a mixed phase can introduce a high abundance of defect sites such as oxygen vaccines, Ti interstitials, and Ti^{3+} in the TiO_2 crystal lattice [10]. TiO_2, with these intrinsic defects, is catalytically more active, compared to pristine TiO_2 [10].

Reports on the interfaces and Fermi levels reveal that the presence of band offsets in the anatase-rutile heterophase, where a built-in electric field was experienced by the photo-generated electrons/holes that could effectively separate the charges [11]. In a recent study, TiO_2 heterophase (with 79 % anatase and 21 % rutile) coated cotton fabrics showed excellent performance for the inactivation of bacteriophage MS2, influenza virus and murine norovirus in a shorter duration of time compared to single phase TiO_2 [12].

Degussa P25 is one of the most widely studied TiO_2 heterophase materials and is widely used for various commercial applications [11]. Various techniques and additives have been used with Degussa P25 to improve charge transfer in TiO_2 heterophase catalysts, to enrich the performance under all light/dark conditions and expand the thermal stability of anatase crystals at high processing temperatures. One of the competent strategies is the incorporation of impurity energy levels into the forbidden band of TiO_2 *via* doping of metal ions at Ti^{4+} sites [13]. The dopants usually have different ionic radius compared to Ti^{4+}, and therefore can influence

the geometry, Ti oxidation state, and the formation of oxygen or Ti vacancies [13]. Ta is a bioactive element and it is commonly used with titanium (Ti) alloys/implants to improve the stability, corrosion resistance and electronic properties [14]. The solubility of Ta^{5+} dopant in TiO_2 matrix is higher, compared to other dopants with +5 oxidation states, for example niobium (Nb) [15] as a result of low energy is required to substitute Ta in the TiO_2 anatase framework. The maximum solid solubility of Ta would be favourable for its uniform distribution in the TiO_2 crystal lattice without deteriorating the crystallization features at low doping concentrations [1]. In addition to that, the energy needed to substitute one Ta atom on a Ti site in the TiO_2 framework is lower than other dopants [15]. The electronic conductivity of Ta doped TiO_2 (Ta-TiO_2) samples arises primarily from the itinerant Ti *d* electrons [15]. Owing to the electronic structure of V_B elements, a donor energy level can be created in the in the forbidden band of TiO_2 to enhance the charge carrier separation [16, 17].

In recent years, Ta-TiO_2 has been investigated for solar cells [18], water splitting [19], corrosion resistance [20], photovoltaics [17], wastewater treatment [8], oxygen reduction reaction [21], and lithium ion batteries [22]. These reports have shown that Ta could be utilised as an effective additive or dopant to increase the catalytic performance of TiO_2. Nevertheless, most of these studies only disclose the extrinsic features of the Ta dopant on improving the catalytic performance of TiO_2. There have been to date no detailed investigations on theoretical calculations of Ta-TiO_2 and on the role of Ta doping on the stability of TiO_2 phases.

With this in mind, the present study, focuses on the impact of Ta doping on the anatase to rutile transition (ART), structural characteristics, and oxygen and Ti vacancies using density Functional Theory (DFT) which are verified with the help of X-ray diffraction (XRD), Raman, and X-ray photoelectron spectroscopy (XPS) techniques. These results show the incorporation of Ta into the anatase phase can retard the anatase to rutile phase transition up to 850ºC, making this material interesting for high temperature applications. Introduction of Ta can produce Ti vacancies to charge compensate the different oxidation states, while formation of O vacancies is enhanced.

2. Experimental:

Synthesis of Ta-TiO_2:

Ta-TiO_2 was synthesized by the sol-gel method with various mol % of Ta (such as 0, 2, 4, 8 and 16 mol %) 12. For example, 0.5 ml of tantalum ethoxide was dissolved in 100 ml of isopropanol to synthesis 2 % Ta-TiO_2. Ta precursor solution was added, dropwise, to the titanium isopropoxide (27.75 ml) and isopropanol mixture (200 ml), under constant stirring.

After that, 200 ml of double distilled water was added dropwise to the above Ta-Ti sol mixture. The resulting white precipitates were dried in an oven at 100 °C for 24 h and then the powders were calcined in a muffle furnace at various temperatures (from 500-900 °C) for 2 h with a ramp rate of 10 °C min.

Characterization:

The anatase to rutile transition (ART), crystallinity, and the average crystallite size of Ta-TiO_2 were investigated by X-Ray Diffraction (XRD, Siemens D500) with Cu Kα radiation (λ= 0.15418 nm). The Spurr equation ($F_R = \frac{1}{1+0.8\,[I_A\,(101)/I_R(110)]}$) was used to analyse the anatase and rutile phase compositions of doped TiO_2. The average crystallite size was estimated from the Scherrer equation. A grating of 300 gr/mm was employed to obtain the Raman spectra at an acquisition time of 3 sec. The bonding interactions, oxygen vacancies and oxidation states of Ta-TiO_2 were examined through X-Ray Photoelectron Spectroscopy (XPS, Thermo-Fisher Scientific Instruments (East Grinstead, UK)) with K-Alpha+ spectrometer.

DFT calculations:

First principles calculations have been performed within DFT as implemented in the Vienna Ab Initio Software Package (VASP.5.4.1)[23, 24] using projector augmented wave (PAW) potentials to describe the core-valence interaction and the Perdew, Burke, Ernzerhof (PBE) generalised gradient approximation to the exchange correlation functional [25, 26]. The potentials for titanium (Ti), oxygen (O) and tantalum (Ta) explicitly account for 4 (d^2s^2), 6 (s^2p^4) and 11($p^6s^2d^3$) valence electrons, respectively. The calculations were executed using an energy cut-off for the plane wave basis set at 420 eV and the convergence criteria for electronic relaxations at 10^{-4} eV and for ionic relaxations at 0.02 eV/Å.

The computed bulk lattice parameters are a = b=3.861 Å and c = 9.781 Å for the anatase phase ($I4_1/amd$) and we used supercells containing 2 x 2 x 2 unit cells (32 atoms). $Ti_{1-x}Ta_xO_2$ was modelled by replacing Ti ions with one, two, three and four Ta ions; these correspond to a 0.03, 0.06, 0.09 and 0.12 mol fraction (x) doping. The TiO_2 supercell is relaxed at each Ta content and no symmetry is imposed. Moreover, in response to this substitution of Ti^{4+} with Ta^{5+} (one extra electron per dopant) the mechanism of charge compensation has been studied through the Ti vacancy formation with four Ta dopants; here each neutral Ti vacancy leaves four holes.

The Brillouin zone was sampled with (2 × 2 × 1) Monkhorst- Pack k-point grids [27]. The calculations were spin-polarised, and no symmetry constraints were imposed. Due to the presence of the extra electron on Ta, we implemented an on-site Hubbard correction (DFT+U) [28] to describe the partially filled Ti 3d states using U = 4.5 eV [29-32].To identify the most stable site for vacancy formation, which is implicated in the transition from the anatase to the rutile phase, different oxygen sites of the Ta-doped structure were considered, taking into account the symmetry of the system. For each oxygen site the vacancy formation energy was computed from the following equation:

$$E_{vac} = E(Ta_xTi_{1-x}O_{2-y}) + {}^1/_2\, E(O_2) - E(Ta_xTi_{1-x}O_2) \quad (1)$$

Where $E(Ta_xTi_{1-x}O_{2-y})$ denotes the total energy of Ta- TiO_2 with a single oxygen vacancy, $E(Ta_xTi_{1-x}O_2)$ represents the total energy of Ta-TiO_2 without an oxygen vacancy and the oxygen vacancy formation energy is referenced to half the total energy of gas-phase O_2. In addition, the oxidation states were analysed through Bader charge analysis [33] and computed spin magnetisations.

3. Results and Discussion:

The effects of Ta dopant in the bulk crystal lattice of anatase TiO_2 on the atomic structure, oxygen vacancy, Ti oxidation state, and lattice parameters were investigated from the DFT calculations. These are validated comprehensively through XRD, and Raman spectroscopic techniques. The introduction of defects, bonding interactions, and other structural changes of TiO_2 were studied by XPS. ART of Ta–TiO_2 was examined in the range of 500-900 °C through determining the anatase and rutile crystalline phase percentages. The distortions of TiO_2 lattice were explored by the Raman analysis. The bare TiO_2 sample (0 % Ta-TiO_2) calcined at 500 and 700 °C was considered as references for pure anatase and rutile, respectively.

3.1. DFT Studies:

Tantalum doped Anatase:

The relaxed structures of Ta- TiO_2 in the most favourable dopant configurations are shown in Figure 1. The doped structure is slightly distorted in the vicinity of the Ta dopant. The Ta−O distances are 2.18 Å for the apical oxygen (O_{ap}) and 2.09 Å for the equatorial oxygen (O_{eq}) sites. The Ta-O_{ap} distance is increased by around 0.20 Å, while the Ta-O_{eq} distance vary by 0.10 Å when compared to the equivalent Ti−O distances in undoped anatase TiO_2. This is consistent with the larger ionic radius of Ta (0.75 Å) compared to Ti (0.61 Å). The lattice

constants with one Ta dopant are a = b = 7.620 Å and c = 19.283 Å. Table 1 shows the computed lattice constant for each Ta doping concentration. In general, substituting a higher concentration of Ta species for Ti results in an increase in the lattice constants.

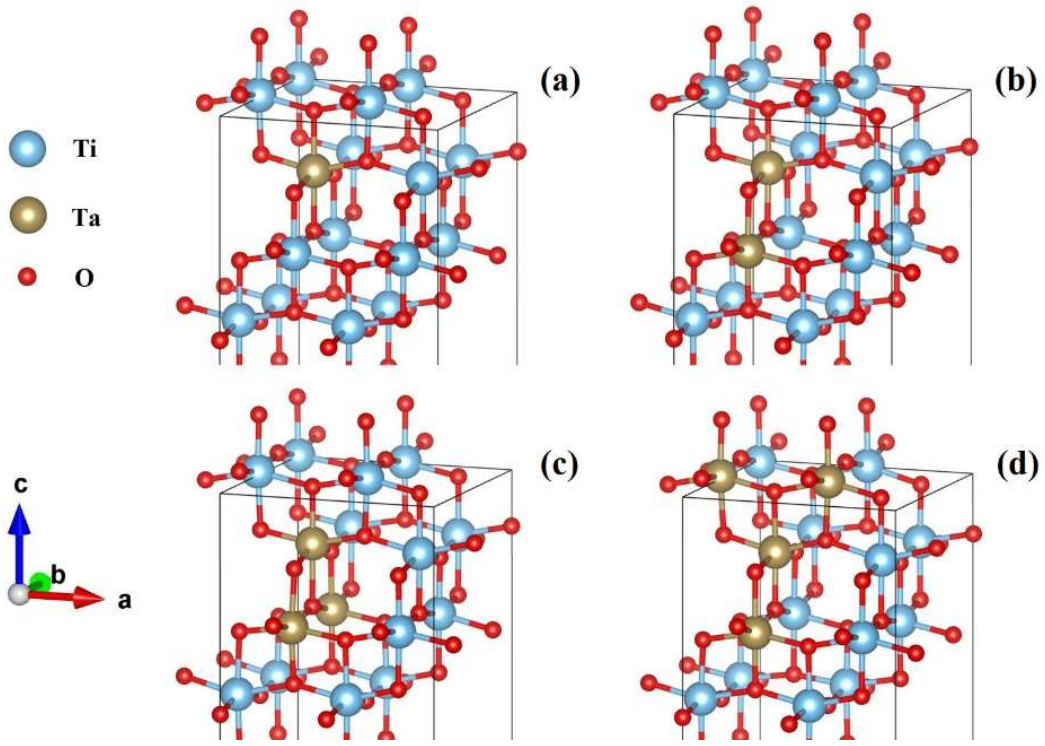

Figure 1. Atomic structures of $Ti_{1-x}Ta_xO_2$ in the most stable configurations for (a) one, (b) two, (c) three and (d) four Ta dopant atoms.

In pure anatase the computed Bader charges on Ti and oxygen are q= 1.45 (giving a net charge of +2.55 electrons) and q = -7.27 electrons (giving a net charge of -1.27 electrons), respectively. Ta can take a variety of oxidation states, from -1 to +5. When one Ta is incorporated into the anatase lattice, the computed Bader charge is q = 8.04 electrons, showing oxidation of Ta, with a net charge of +2.96 electrons and a computed spin magnetisation of 0.02 μ_B. Oxygen apical sites in the vicinity of Ta shows a modest decrease in the Bader charge to *ca.* 7.25 electrons, with a negligible spin magnetization.

At the same time, the nearest adjacent Ti atom shows an increase in the Bader charges of 0.31 electrons, while the Bader charges of the other six neighboring Ti atoms increases by 0.10 electrons. This analysis suggests that the Ta dopant is fully oxidized, with localization of the electron on the adjacent Ti atom and partial localization of the electron over six Ti sites.

Upon increasing the Ta concentration, the Bader charge of Ta and Ti atoms show oxidation of Ta (change in charge of 0.75 electrons) and reduction of Ti (change in charge of *ca.* 0.40 electrons). The magnetization of the $Ti_{1-x}Ta_xO_2$ is mainly attributed to the magnetization of each Ti atom that is nearest neighbor to Ta, with computed magnetisations of *ca.* 1.0 μ_B.

Table 1 Summary of computed lattice constants, computed Bader charges and spin magnetizations for Ta-TiO_2 anatase with different Ta contents.

Ta concentration	**3%**	**6%**	**9%**	**12%**
Lattice Constants (Å)	a = b = 7.757 c = 19.150	a = b = 7.766 c = 19.194	a = 7.795 b = 7.803 c = 19.193	a = 7.779 b = 7.781 c = 19.286
Bader Charge Ta (e^-)	Ta^1 = 8.04	Ta^1 = Ta^2 = 8.12	Ta^1 = 8.01 Ta^2 = 8.47 Ta^3 = 8.22	Ta^1 = 8.69 Ta^2 = 8.79 Ta^3 = Ta^4= 8.63
Bader Charge Ti – NN (e^-)	Ti^1 = 1.75	Ti^1 = Ti^2 = 1.82	Ti^1 = 1.82 Ti^2 = 1.85 Ti^3 = 1.87	Ti^1 = 1.95 Ti^2 = 2.05 Ti^3 = Ti^4 = 2.13
Magnetization - Ti – NN (μ_B)	Ti^1 = 0.96	Ti^1 = Ti^2 = 0.96	Ti^1 = 0.97 Ti^2 = 0.99 Ti^3 = 0.98	Ti^1 = 0.99 Ti^2 = 0.98 Ti^3 = 0.97 Ti^4 = 0.99
Bader Charge Ti – N (e^-)	1.45 – 1.55	1.46 – 1.62	1.54 – 1.72	1.50 – 1.88
Bader Charge O (e^-)	7.23 – 7.30	7.18 – 7.27	7.13 – 7.30	7.05 – 7.15

Oxygen Vacancy Formation in Ta-doped TiO_2

Figure 2 shows the structures with the lowest computed formation energies for an oxygen vacancy in $Ti_{1-x}Ta_xO_2$ (Ta concentration = 3 % Figure 2(a), 6 % 2(b), 9 % 2(c) and 12 % 2(d)).

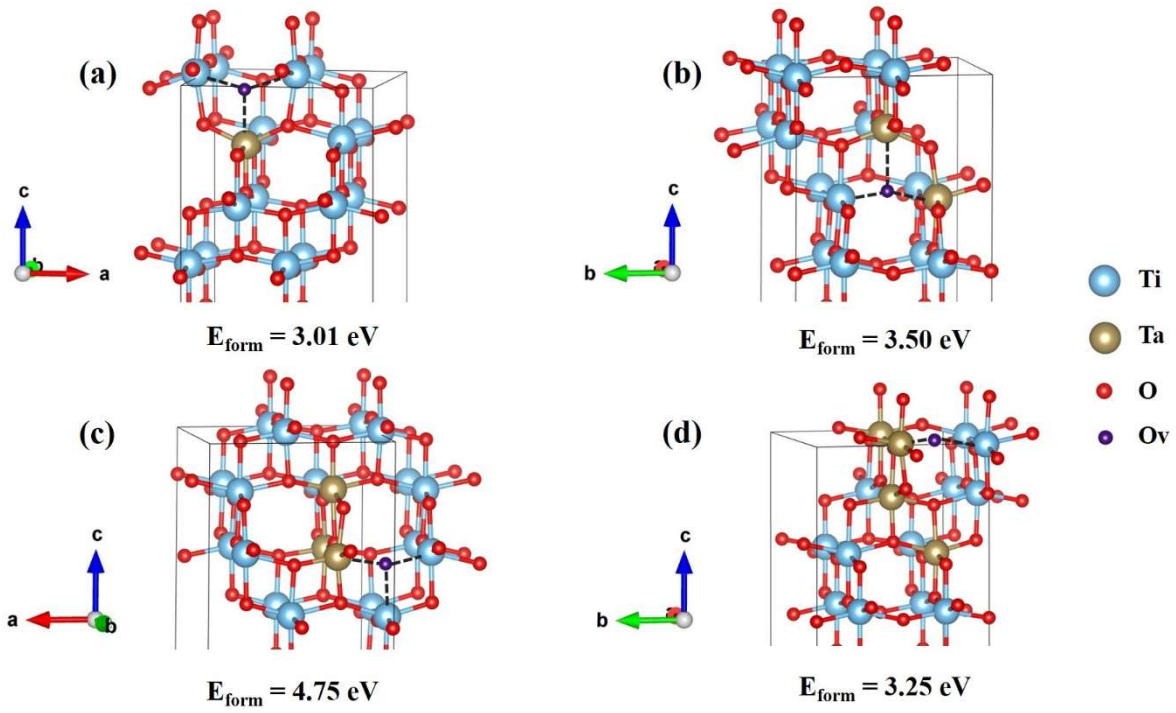

Figure 2. Position of Oxygen vacancy (O_v) in Ta- TiO_2 anatase structure at different dopant concentrations and respective energy formation. The bonds formed before the O was removed are dashed.

The positive computed oxygen vacancy formation energy means that the creation of the oxygen vacancy is in principle not spontaneous. It is nonetheless sufficiently small that an oxygen vacancy can form at high calcination temperatures. In addition, this vacancy formation energy is, apart from the 9 % Ta concentration, reduced with respect to the formation energy of an oxygen vacancy in the undoped anatase supercell, for which we compute an oxygen vacancy formation energy of 3.83 eV.

After vacancy formation, the lattice of $Ti_{1-x}Ta_xO_2$ shows some structural distortions. In the most favourable oxygen vacancy structure, Ta, Ti, and neighboring oxygen ions distort from their initial positions. For $Ti_{1-x}Ta_xO_2$ with 3 % of Ta concentration, the most favourable oxygen vacancy structure is the configuration in which vacancy was an O in apical position. In this configuration, both Ta and the two Ti atoms moves away from the vacancy, in particular, the Ta – O_{eq} and Ta – O_{ap} distances are decreased by 0.06 Å and 0.11 Å, respectively. The Ti neighboring oxygen atoms in the apical positions tilt towards the vacancy, Ti – O_{ap} distances are increased by 0.08 Å, while the remaining Ti – O_{eq} distances are not distorted.

After the formation of oxygen vacancy for 3 % Ta doping, the computed Bader charge for Ta shows a small change, from q = 8.04 to q = 8.10 electrons, and the change in the spin

magnetisation in the d-orbital is negligible. The two nearest neighbour Ti ions to which the removed O was bound now have computed spin magnetisations of 0.96 μ_B and a computed Bader charge of 1.90 electrons, while the Bader charge of Ti adjacent Ta increases by 0.02 electrons and the magnetization to 1.0 μ_B, so the total magnetization is ca. 3 μ_B.

In $Ti_{1-x}Ta_xO_2$ structures at higher Ta concentration, the computed Bader charge of Ta is increased from q = 8.20 to q = 8.88 electrons as the Ta concentration is increased from 6 to 12%. After formation of oxygen vacancy, the total magnetization on Ta is not negligible, in particular we see values of 0.15 μ_B at 6 %, 0.10 μ_B at 9 % and 0.14 μ_B at 12% Ta. The Bader charge of the Ti ions surrounding Ta increases from q = 2.09 to q = 2.36 electrons, while the total magnetization of Ti increases, with a value of 3.2 μ_B over three Ti atoms at 6 % and over five Ti atoms at 9 % and a value of 3.5 μ_B over five Ti atoms at 12 %.

Titanium Vacancy Formation in Ta-doped Anatase

To analyse the compensation of the different Ti and Ta oxidation states in $Ti_{1-x}Ta_xO_2$ at 12 % Ta, we have considered the formation of one Ti vacancy. Here each neutral Ti vacancy leaves four holes which compensate the four electrons introduced by the Ta dopants (one electron per dopant). The computed formation energy, relative to the energy of a single Ti atom in the bulk metal ($E^{Ti\ Vac} = E(TaTi_{1-x}O_2) + E(Ti) - E(TaTiO_2)$, where E(Ti) is the energy of one Ti atom from bulk Ti metal) is -2.57 eV, confirming that Ti vacancies will form to compensate higher Ta dopant concentrations.

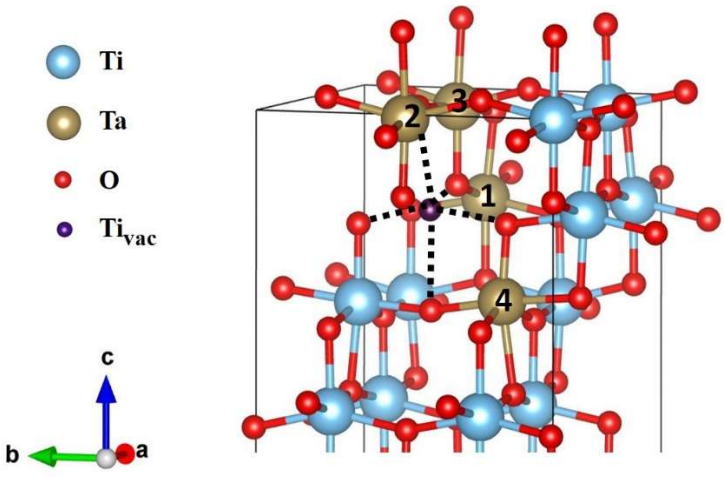

Figure 3. The position of titanium vacancy (Ti_{vac}) in $Ti_{1-x}Ta_xO_2$ at 12 % of Ta concentration

After the formation of Ti vacancy, Ta atoms move close the vacancy especially the Ta ions indicated as Ta^1 and Ta^4 in Figure 3; these ions also have Bader charge lower by 0.13 electrons than Ta^2 and Ta^3. In this configuration Bader charge of Ta ions is lower by ca. 0.75 electrons with respect to $Ti_{1-x}Ta_xO_2$ at 12 % Ta without the Ti vacancy. In addition, Ti atoms have Bader charge lower than the prior system with values between 1.48 and 1.78 electrons and no magnetization is present. This confirms the compensation of the difference in Ti and Ta oxidation states.

Electronic Structure of Tantalum-Doped TiO_2

The computed projected electronic density of states (PEDOS) for bulk TiO_2 in anatase phase, compared with the total density of states (TDOS) of Ta-doped and with oxygen vacancy at different Ta concentration, are shown in **Figure 4** and **Figure S1,** respectively.

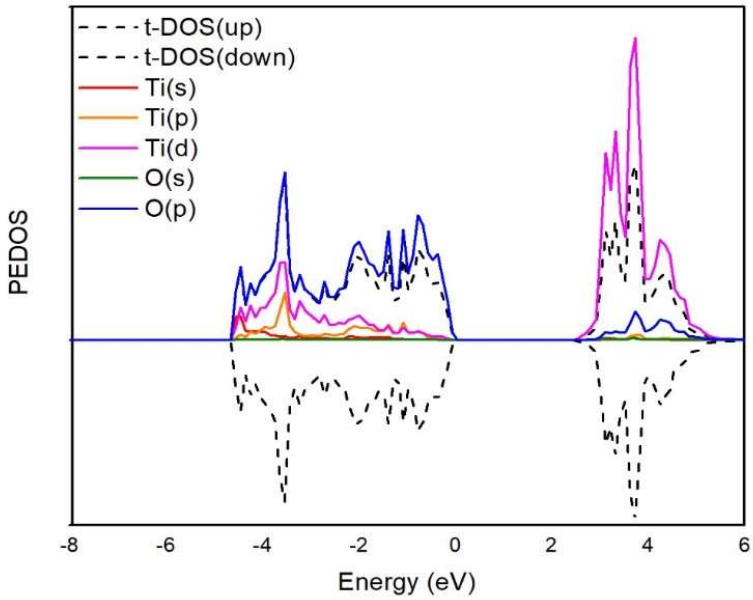

Figure 4. The calculated total and partial density of states of pure TiO_2 in the anatase phase. Only the total DOS is shown for the spin down electrons.

After Ta doping, states emerge in the band gap region of bulk TiO_2 above the valence band maximum (VBM). These correspond principally to Ti 3*d*-orbitals as shown in the left panel of **Figure S.I.**. In particular, these states are localized at 0.95, 0.96, 0.48 and 0.64 eV above the VBM in Ta-doped TiO_2.

In these configurations, after formation of the oxygen vacancy results in the formation of further occupied Ti 3*d* states in the band gap, as shown in right panel of **Figure 5**. The

bandgap is reduced by 1.26, 1.42, 1.59 and 1.74 eV for Ta doping at the concentration of 3, 6, 9 and 12 % respectively.

The consequence of charge compensation in the case of Ti vacancy in TiO_2 doped with four Ta atoms, was reinforced by analysing the DOS, from which no localized states are found in the VB – CB energy gap, as shown in **Figure 6**.

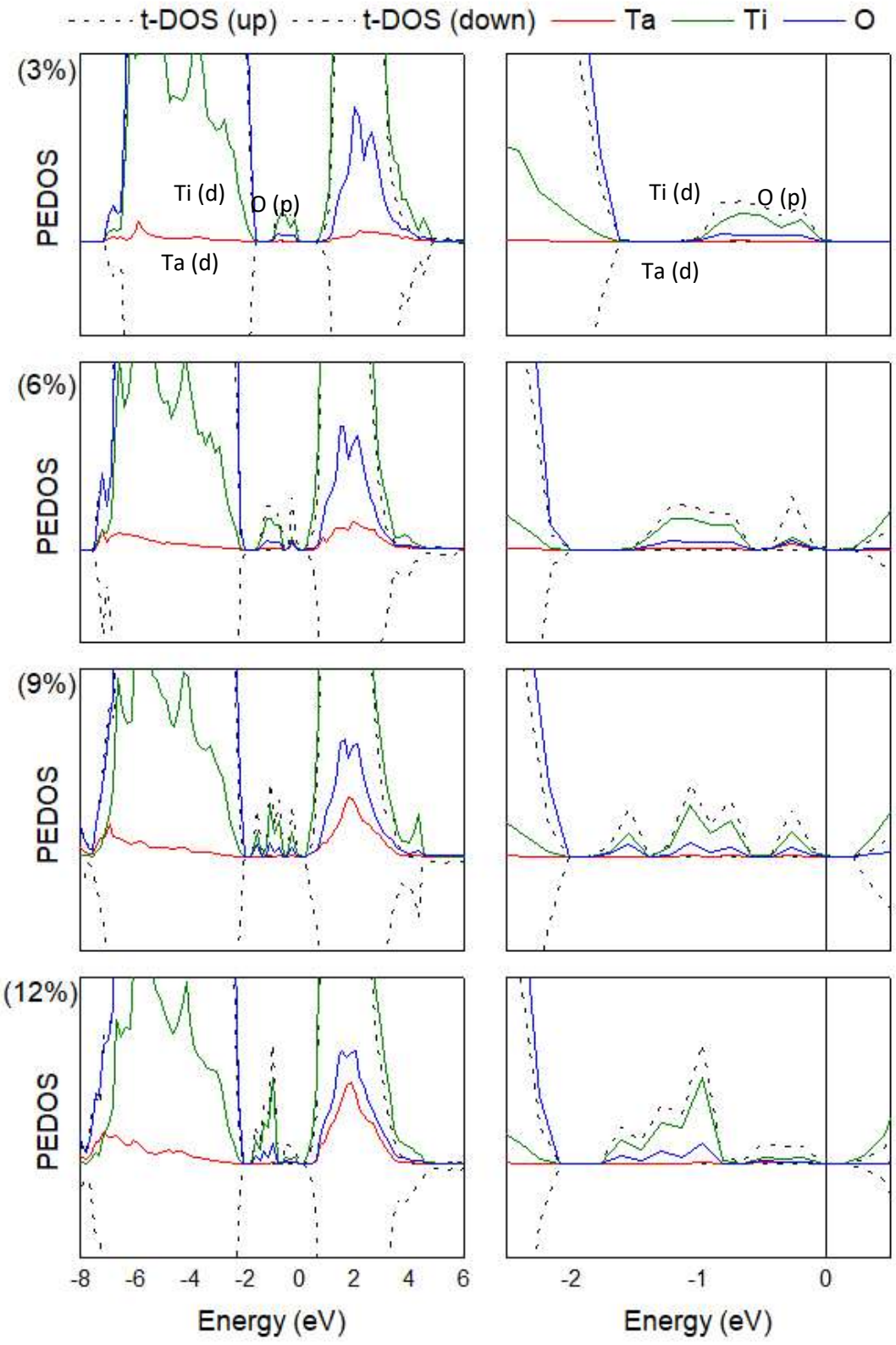

Figure 5. The calculated partial density of states (**left panels**) and bandgap region (**right panels**) of $Ti_{1-x}Ta_xO_2$ with oxygen vacancy at different concentrations. Fermi level is set at zero.

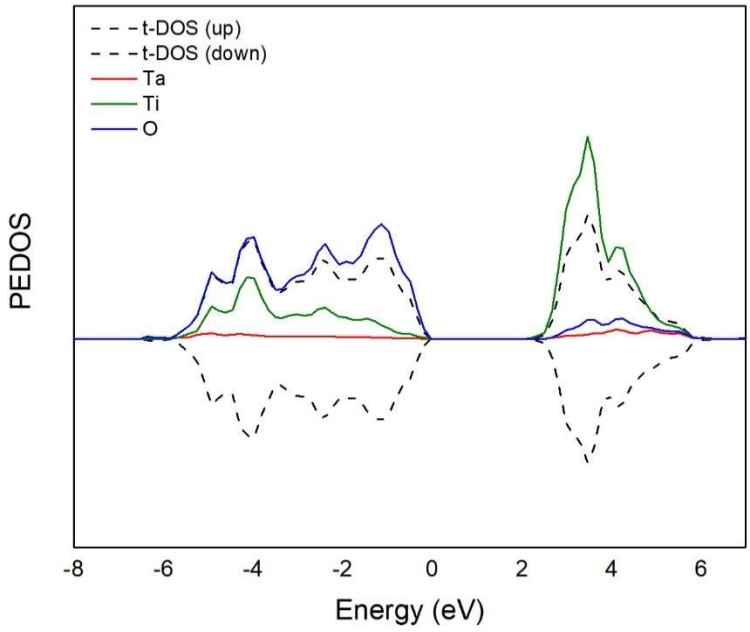

Figure 6. The calculated PEDOS with titanium vacancy of $Ti_{1-x}Ta_xO_2$ at 12 % of Ta concentration

3.2. XRD:

The diffraction peaks of Ta-TiO_2 samples calcined at various temperatures are shown in **Figure 7**. The effect of Ta doping is evidenced through the variations in peak position, width, and intensity. The anatase and rutile phase percentages of TiO_2 are displayed in Table 2. Ta doping can preserve the anatase up to 850 °C. The crystalline phases of orthorhombic tantalum oxide (Ta_2O_5) are observed at high Ta concentration (8 and 16 mol %). For samples calcined at 800, 850 and 900 °C, the 2θ peaks at 22.5, 28.35, 36.96, 49.83, and 50.97 are attributed to the presence of (001), (1110), (1111), (0220), and (2151) orthorhombic phases of Ta_2O_5 [8, 34]. Ta_2O_5 formation is increased with respect to the temperature and Ta content, demonstrating the robust reduction reaction at high temperatures [13]. The crystallization of amorphous to orthorhombic Ta_2O_5 occurs at temperatures above 800 °C.

The broadening of XRD peaks signifies the decrease of average crystallite size of TiO_2 with respect to the Ta concentration. A slight peak shift is also observed at high dopant concentration, indicating the incorporation of Ta^{5+} in the crystal lattice of TiO_2 [35]. The atomic radius of Ta^{5+} is slightly bigger than that of Ti^{4+}, and therefore the substitution of Ta could lead to an enlargement of TiO_2 unit cell [36].

The average crystallite size of anatase, rutile and Ta-TiO_2 samples are given Table 3. With respect to the calcination temperature, the size of nanoparticles is increased. Conversely, the average crystallite size of the samples is decreased with respect to Ta concentration. This

is attributed to the impact of Ta^{5+} dopant to inhibit the grain boundary mobility [37]. The effect of doping on the crystal growth of TiO_2 is dominant at low Ta concentration.

The decrease of crystallite size with respect to the concentration of Ta is ascribed to the solute drag mechanism [36]. According to this mechanism, the difference in size between the dopant and Ti ions will induce lattice strain energy (ΔG_{strain}) in the TiO_2 crystal. ΔG_{strain} with electrostatic potential energy could increase the interaction between the grain boundary and the dopant. Consequently, the grain growth of Ta-TiO_2 samples is significantly suppressed due to the size mismatch. The crystal lattice parameters are influenced by the band length difference between the covalent Ti-O (2.01 Å) and Ta-O (2.17 Å) bands [15]. The decrease of average crystallite size is also attributed to the quantum size effects resulting from the small sized anatase nanoparticles at high Ta content [38].

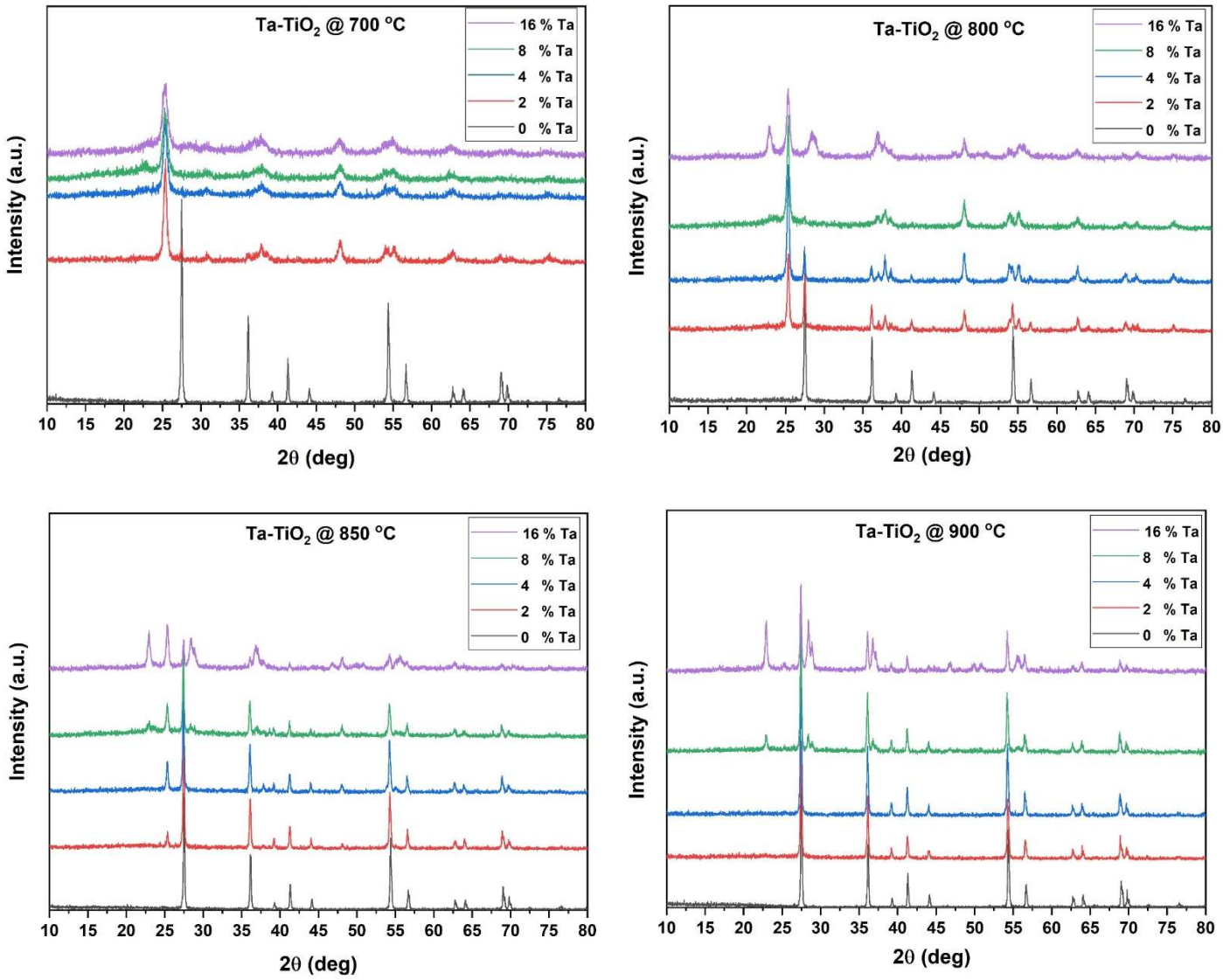

Figure. 7. XRD patterns of Ta-TiO_2 at various calcination temperatures

Table 2. Anatase and Rutile percentages of Ta-TiO_2 samples at various calcination temperatures

Samples	500 °C		600 °C		700 °C		800 °C		850 °C		900 °C	
	A	R	A	R	A	R	A	R	A	R	A	R
0 % Ta-TiO_2	100	-	8	92	-	100	-	100	-	100	-	100
2 % Ta-TiO_2	100	-	100	-	82	18	53	47	12	88	-	100
4 % Ta-TiO_2	100	-	100	-	100	-	72	28	19	81	-	100
8 % Ta-TiO_2	100	-	100	-	100	-	100	-	25	75	-	100
16 % Ta-TiO_2	100	-	100	-	100	-	100	-	54	46	11	89

Table 3. Average crystallite size of Ta-TiO_2 samples at various calcination temperatures

Samples	500 °C	600 °C		700 °C		800 °C		850 °C	
	A (nm)	A (nm)	R (nm)	A (nm)	R (nm)	A (nm)	R (nm)	A (nm)	R (nm)
0 % Ta-TiO_2	13.61	20.17	35.92	-	38.10	-	39.16	-	41.21
2 % Ta-TiO_2	6.74	11.23	-	14.67	25.74	24.73	34.42	28.79	30.08
4 % Ta-TiO_2	5.71	6.51	-	12.86	-	23.16	35.54	28.26	37.59
8 % Ta-TiO_2	5.10	6.75	-	9.72	-	18.92	-	19.84	36.37
16 % Ta-TiO_2	5.48	5.16	-	7.81	-	14.63	-	19.27	34.57

3.3. Raman:

There are no significant changes in the Raman peak positions for Ta-TiO_2 calcined at 800 °C. However, a slight red shift in peak position is noted for the samples calcined at 850 °C (**Figure 8**). This is ascribed to the expansion of unit cell and lattice parameter variations with respect to Ta doping and calcination temperature [36]. B_{1g} peak responsible for the Ti-O stretching mode (~390 cm^{-1}) is blue shifted with respect to the Ta concentration, suggesting the substitutional doping of Ta ions in the TiO_2 crystal lattice [35]. A slight red shift of E_g peak is noted for the samples calcined at 850 °C. The widening and shifting of E_g peaks are attributed to the formation of new Ta bonds *via* disturbing the Ti-O-Ti bonds in the crystal lattice. E_g peak typically depicts the symmetric stretching vibration of O-Ti-O in TiO_2. Ta-O-Ti or Ta-O-Ta bonds are formed as the Ta^{5+} is substitutionally doped on Ti^{4+} sites[39]. Raman peak shapes could be influenced by the non-stoichiometry. The incorporation of Ta^{5+} ions could create intrinsic defects to retain the charge neutrality, which could cause local lattice distortion [40]. The decrease in crystallite size could also lead to the Raman peak shit and broadening [40]. Phonon confinement effect could also be considered for the doped samples with low particle size compared to the pure TiO_2 [40].

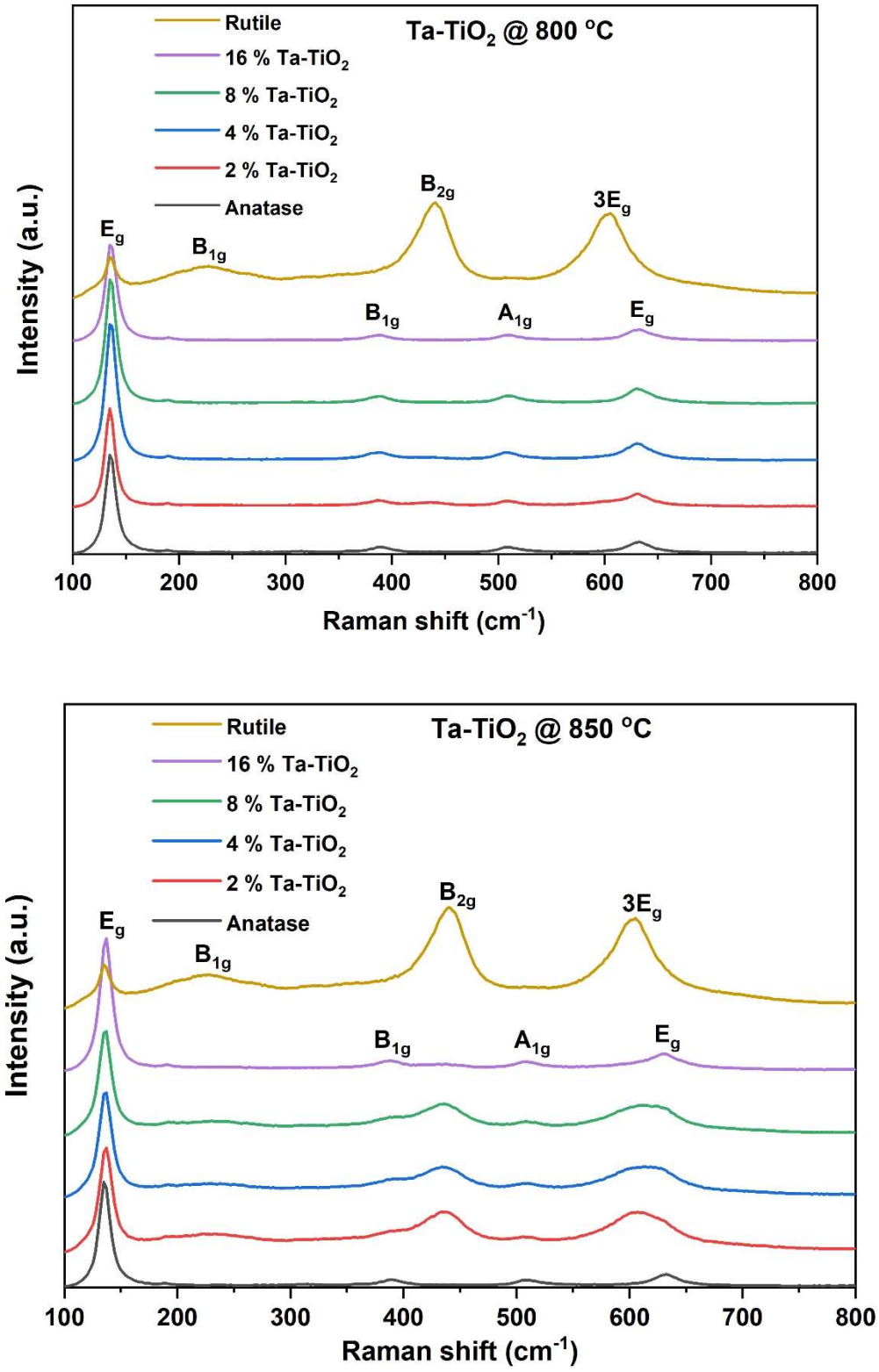

Figure. 8. Raman spectra of Ta-TiO_2 at 800 °C and 850 °C

3.4. XPS:

XPS results of TiO_2 anatase and Ta-TiO_2 samples are shown in **Figure 9 and 10**. The characteristic peaks of Ti^{4+} appear as doublet around 458.78 eV and 464.48 eV for $2p_{3/2}$ and $2p_{1/2}$ states, respectively [35] (**Figure. 9 (a)**). Ti 2p and O 1s peaks are slightly red shifted after doping with Ta. An additional peak in the Ti 2p spectrum of Ta-TiO_2 is attributed to the existence of Ti^{3+}. Ta doping generates Ti^{3+} defect states in the crystal lattice (**Figure. 9 (c)**). An extra positive charge might be introduced into the TiO_2 system by the doping of Ta^{5+} ions. This charge imbalance in the crystal lattice can be compensated through the formation of reduced Ti^{3+} [17]. The atomic radius of Ti^{3+} (0.67 Å) is larger than that of Ta^{5+} (0.64 Å).

In the case of the Ta spectrum, the peaks at 26.36 and 28.25 eV are attributed to the Ta $4f_{7/2}$ and Ta $4f_{5/2}$ states, respectively. These peaks are assigned to Ta^{5+}. A small peak observed at 22.45 eV is ascribed to O 2s [21].

The peaks at 531.85 and 532.67 eV are attributed to the existence of Ti-O and Ti-OH groups, respectively. The increase in binding energy of O 1s peaks could be attributed to the existence of Ta-O bonds in the doped samples [41]. The ratio of oxygen vacancies depends on the concentration of Ta. Moreover, at high temperatures, more oxygen atoms could enter into the crystal lattice and occupy the vacancies, leading to lattice expansion [13]. This is also validated by the changes in XRD peak intensity, width, and position.

The formation of oxygen vacancies and Ti^{3+} ions are described as follows [36]:

$$2TiO_2 + Ta_2O_5 \rightleftharpoons 2Ti'_{Ti} + 2Ta_{Ti}^{\cdot} + 8O_o + O_2 \uparrow$$

$$O_o \rightleftharpoons 2e^- + V_o^{\cdot\cdot} + \frac{1}{2} O_2 \uparrow$$

$$Ti^{4+} + e^- \rightleftharpoons Ti^{3+}$$

Here, " $'$ ", " $^{\bullet}$ ", and $V_o^{\cdot\cdot}$ represent an extra negative charge, extra positive charge, and oxygen vacancies with positive charge, respectively. At low dopant concentration, the substitution of Ta^{5+} and the formation of $V_o^{\cdot\cdot}$ instigate the reduction of Ti^{4+} to Ti^{3+}. The concentration of Ti^{3+} is increased with respect to the concentration of Ta. Nevertheless, the excessive electrons at high Ta contents can be captured by $V_o^{\cdot\cdot}$ to further convert into O_o, leading to a decrease in concentration of oxygen vacancies. This reverse reaction would decrease the concentration of electrons and restrain the Ti^{3+} content at very high Ta doping levels.

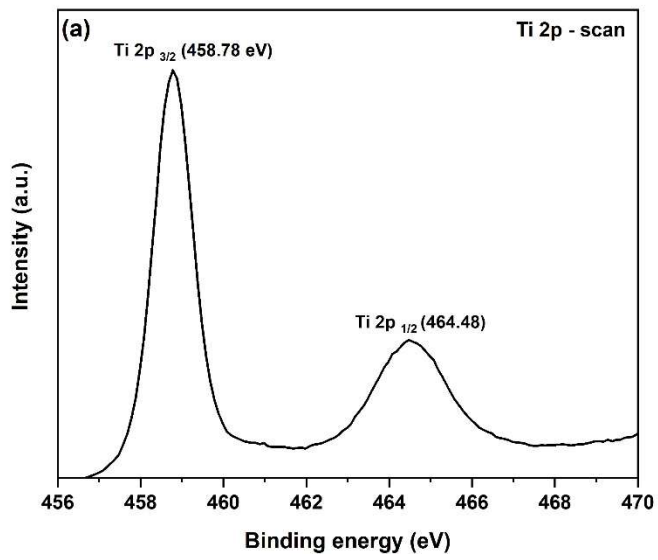
(a)
Ti 2p - scan
Ti 2p 3/2 (458.78 eV)
Ti 2p 1/2 (464.48)
Intensity (a.u.)
Binding energy (eV)
456
458
460
462
464
466
468
470

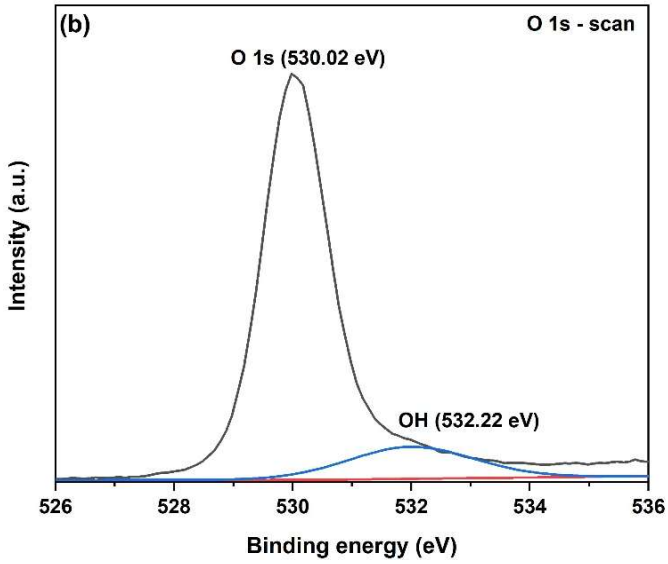
(b)
O 1s - scan
O 1s (530.02 eV)
OH (532.22 eV)
Intensity (a.u.)
Binding energy (eV)
526
528
530
532
534
536

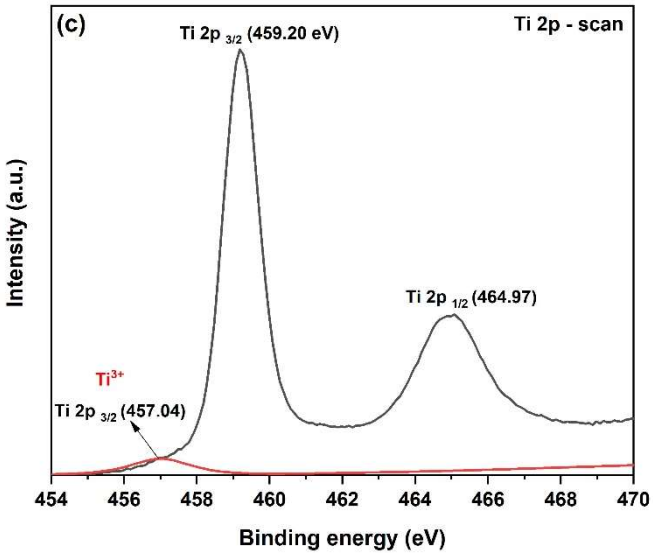
(c)
Ti 2p - scan
Ti 2p 3/2 (459.20 eV)
Ti 2p 1/2 (464.97)
Ti3+
Ti 2p 3/2 (457.04)
Intensity (a.u.)
Binding energy (eV)
454
456
458
460
462
464
466
468
470

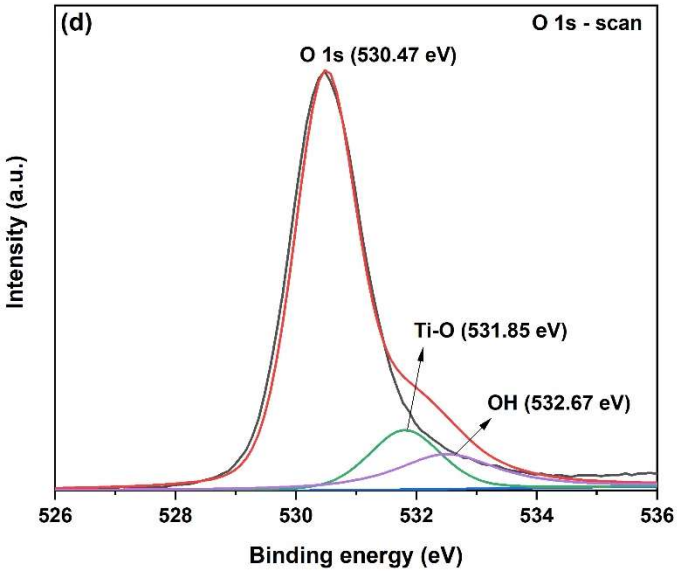
(d)
O 1s - scan
O 1s (530.47 eV)
Ti-O (531.85 eV)
OH (532.67 eV)
Intensity (a.u.)
Binding energy (eV)
526
528
530
532
534
536

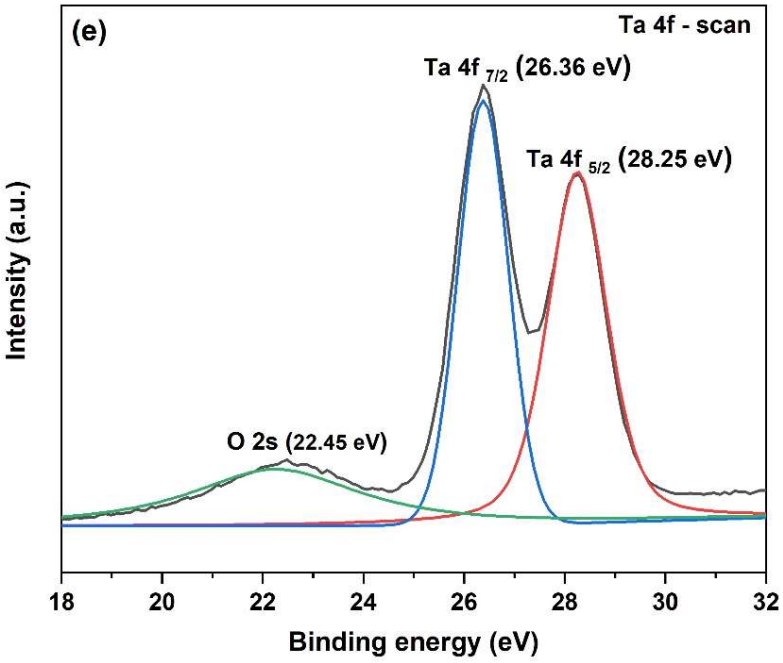
(e)
Ta 4f - scan
Ta 4f 7/2 (26.36 eV)
Ta 4f 5/2 (28.25 eV)
O 2s (22.45 eV)
Intensity (a.u.)
Binding energy (eV)
18
20
22
24
26
28
30
32

Figure. 9. XPS of TiO_2 anatase ((a) Ti 2p and (b) O 1s) and 4 % Ta-TiO_2 at 800 °C ((c) Ti 2p, (d) O 1s, and (e) Ta 4f)

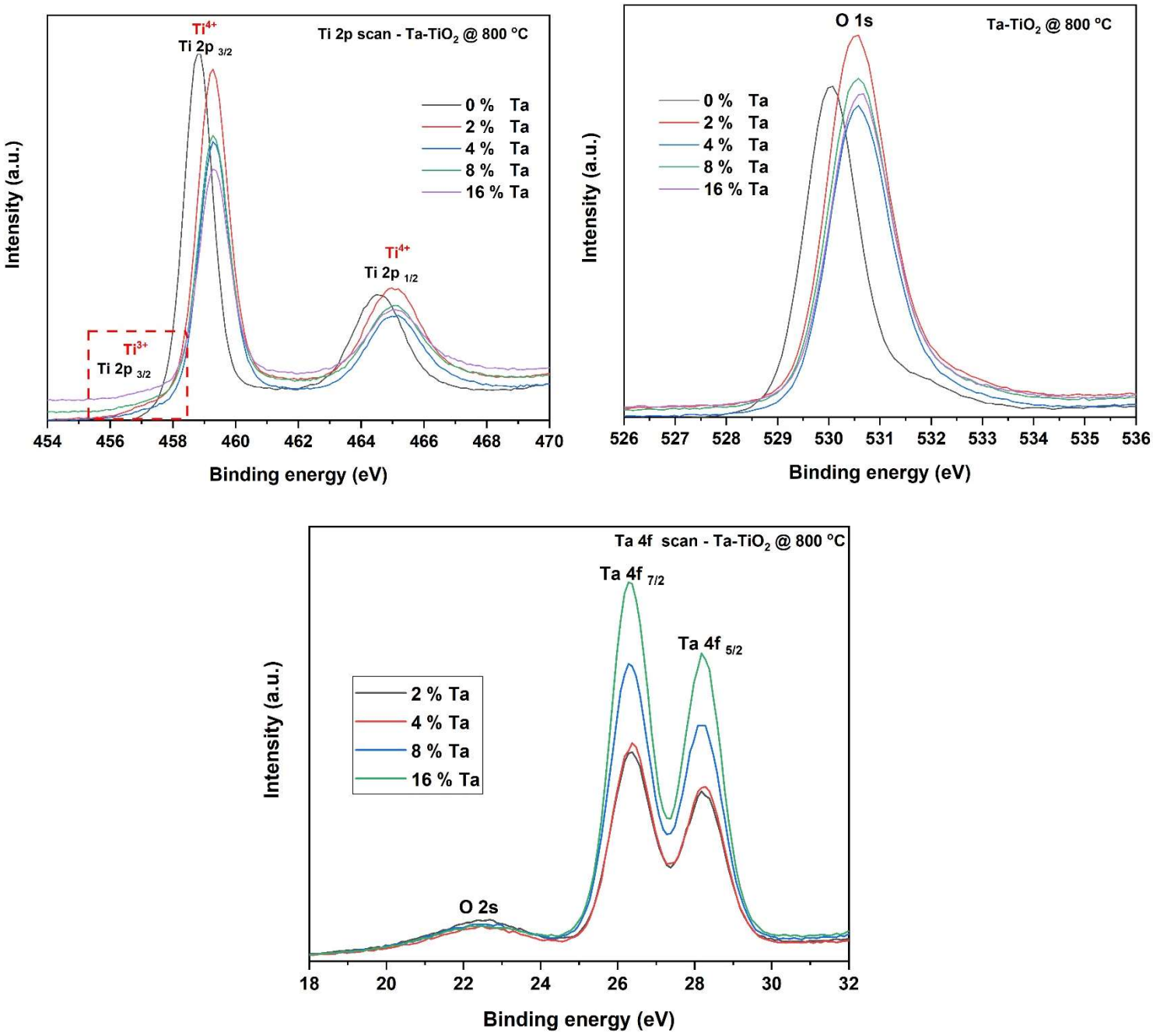

Figure. 10. XPS scans of 4 % Ta-TiO_2 at 800 °C

The substitution of Ti^{4+} by the Ta^{5+} ions could increase the electron concentration in the crystal lattice along with the formation of Ti^{3+} defect states. These defect states could introduce new energy levels below the conduction of TiO_2 to enhance charge transfer and the light absorption. The defects at low Ta concentration could increase the photocatalytic activity of TiO_2 but the defects could also act as charge-carrier recombination centres at higher concentrations. The charge carrier mobility would be decreased at high Ta concentrations due to the distortion of TiO_2 crystal lattice [15]. Sing *et al.* suggested that the an optimum Ta content in TiO_2 was responsible for the surface enhanced Raman scattering (SERS) to enrich the charge transfer mechanism on the catalyst surface [35].

The changes in lattice parameters might be attributed to the introduction of Ta^{5+} and the transition of Ti^{4+}. The size of Ta^{5+} and Ti^{3+} ions is slightly larger than that of Ti^{4+} ions, and therefore the Ta-TiO_2 crystal lattice is slightly distorted. Mott-Schottky results of a recent study proved that the charge carrier density of Ta-TiO_2 is 3.2 times higher than that of pure TiO_2 [17]. Consequently, Ta-TiO_2 could be utilised as a promising material for hydrogen production through photocatalytic or photoelectrocatalytic water splitting owing to the high photocurrent density and charge transfer.

It was suggested that the increase of calcination temperature and Ta content could favour the grain boundary facets [42]. According to the Krogar-Vink notation, the incorporation of Ta in TiO_2 under different conditions can be described as follows [42]:

At oxidising condition:

$$2Ta_2O_{5(s)} \leftrightarrow 4Ta_{Ti}^{\bullet} + V_{Ti}'''' + 10O_o^x$$

$$[Ta_{Ti}^{\bullet}] = 4[V_{Ti}'''']$$

At reducing condition:

$$2Ta_2O_{5(s)} \leftrightarrow 4Ta_{Ti}^{\bullet} + 4e' + 8O_o^x + O_{2(g)}$$

$$[Ta_{Ti}^{\bullet}] = n$$

Here, $Ta_{Ti}^{\bullet}$, V_{Ti}'''', and O_o^x signify a substitutional Ta^{5+} ion in a regular Ti lattice site, quadruply charged Ti vacancy, and a regular neutral oxygen species on an oxygen site, respectively. Under oxidising conditions, the incorporation of Ta is charge compensated through Ti vacancies and ionic species. Here, the diffusion of Ta is accompanied by the diffusion of Ti vacancies, which is a particularly slow process. Under oxidising conditions, the incorporation of Ta is charge compensated by electrons. In contrast, the diffusion of Ta is accompanied by electrons with high mobility under reducing conditions [42]. It was suggested that, under

oxidising conditions, Ta^{5+} ions could be enriched on the surface of Ta-TiO_2 due to the slow diffusion kinetics [42].

4. Conclusions:

The influence of Ta doping on the structural and electronic properties of TiO_2 has been successfully investigated. To retain the charge neutrality Ti^{3+} defect states were generated during the substitution of Ta^{5+} in the TiO_2 crystal lattice, while at high Ta content Ti vacancies can form to charge compensate the dopant. The formation of intrinsic defects could cause local lattice distortion. The average crystallite size of TiO_2 decreased with respect to Ta content and at the same time, it increased as the temperature increases. The crystallite size measurements also revealed the impact of Ta^{5+} dopant on the grain boundary mobility. The ratio of oxygen vacancies was also influenced by the Ta dopant concentration and calcination temperature. Ta dopant preserved the anatase content at high calcination temperatures and the 4 % Ta-TiO_2 calcined at 800 °C exhibited 72 % anatase and 28 % of rutile. The incorporation of Ta in TiO_2 under oxidising and reducing conditions has been discussed. The incorporation of Ta is charge compensated through Ti vacancies and ionic species under the oxidising conditions. The diffusion of Ta is accompanied by electrons with high mobility under the reducing conditions.

Acknowledgement:

The authors (VK, SM, JB and SCP) would like to thank the European Union's INTERREG VA Programme for the Renewable Engine (RE) project, managed by the Special EU Programmes Body (SEUPB), with match funding provided by the Department for the Economy (Northern Ireland) and Department of Business, Enterprise and Innovation (Republic of Ireland). MBM and MN acknowledge access to computing resources at Irish Centre for High End Computing (ICHEC).

References:

1. Zhao, W.; He, L.; Feng, X.; Xiao, H.; Luan, C.; Ma, J., Deposition and characterization of epitaxial Ta-doped TiO2 films for ultraviolet photoelectric detectors. *Ceramics International* **2018,** *44* (17), 21114-21119.
2. Medvids, A.; Onufrijevs, P.; Kaupužs, J.; Eglitis, R.; Padgurskas, J.; Zunda, A.; Mimura, H.; Skadins, I.; Varnagiris, S., Anatase or rutile TiO2 nanolayer formation on Ti substrates by laser radiation: Mechanical, photocatalytic and antibacterial properties. *Optics & Laser Technology* **2021,** *138*, 106898.
3. Kumaravel, V.; Mathew, S.; Bartlett, J.; Pillai, S. C., Photocatalytic hydrogen production using metal doped TiO2: A review of recent advances. *Applied Catalysis B: Environmental* **2019,** *244*, 1021-1064.
4. Hosseini, Z.; Shasti, M.; Ramezani Sani, S.; Mortezaali, A., Photo-detector diode based on thermally oxidized TiO2 nanostructures/p-Si heterojunction. *Journal of Applied Physics* **2016,** *119* (1), 014503.
5. Avram, D.; Cojocaru, B.; Tiseanu, C., First evidence from luminescence of lanthanide substitution in rutile TiO2. *Materials Research Bulletin* **2021,** *134*, 111091.
6. Yamada, Y.; Kanemitsu, Y., Determination of electron and hole lifetimes of rutile and anatase TiO2 single crystals. *Applied Physics Letters* **2012,** *101* (13), 133907.
7. Luttrell, T.; Halpegamage, S.; Tao, J.; Kramer, A.; Sutter, E.; Batzill, M., Why is anatase a better photocatalyst than rutile?-Model studies on epitaxial TiO2 films. *Scientific reports* **2014,** *4* (1), 1-8.
8. Merenda, A.; Kong, L.; Fahim, N.; Sadek, A.; Mayes, E. L.; Hawley, A.; Zhu, B.; Gray, S. R.; Dumee, L. F., Sub-10-nm mixed titanium/tantalum oxide nanoporous films with visible-light photocatalytic activity for water treatment. *ACS Applied Nano Materials* **2019,** *2* (4), 1951-1963.
9. Liu, Y.; Zou, X.; Li, L.; Shen, Z.; Cao, Y.; Wang, Y.; Cui, L.; Cheng, J.; Wang, Y.; Li, X., Engineering of anatase/rutile TiO2 heterophase junction via in-situ phase transformation for enhanced photocatalytic hydrogen evolution. *Journal of Colloid and Interface Science* **2021,** *599*, 795-804.
10. Chen, X.; Peng, X.; Jiang, L.; Yuan, X.; Fei, J.; Zhang, W., Photocatalytic removal of antibiotics by MOF-derived Ti3+-and oxygen vacancy-doped anatase/rutile TiO2 distributed in a carbon matrix. *Chemical Engineering Journal* **2021**, 130945.
11. Asjad, M.; Arshad, M.; Zafar, N. A.; Khan, M. A.; Iqbal, A.; Saleem, A.; Aldawsari, A., An intriguing case of morphology control and phase transitions in TiO2 nanostructures with enhanced photocatalytic activity. *Materials Chemistry and Physics* **2021,** *265*, 124416.
12. Kim, M. G.; Kang, J. M.; Lee, J. E.; Kim, K. S.; Kim, K. H.; Cho, M.; Lee, S. G., Effects of Calcination Temperature on the Phase Composition, Photocatalytic Degradation, and Virucidal Activities of TiO2 Nanoparticles. *ACS omega* **2021,** *6* (16), 10668-10678.
13. Sun, X.-y.; Liu, C.; Chen, Z.; Ma, Y.-q., The photocatalytic performance of Ta and Rh co-doped TiO2 tuned by the average dopant valence. *Materials Research Bulletin* **2018,** *100*, 153-160.
14. Azadmanjiri, J.; Wang, J.; Berndt, C. C.; Kapoor, A.; Ang, A. S.; Srivastava, V. K., Influence of charged defects on the interfacial bonding strength of tantalum-and silver-doped nanograined TiO 2. *Physical Chemistry Chemical Physics* **2017,** *19* (19), 11881-11891.
15. Bawaked, S. M.; Sathasivam, S.; Bhachu, D. S.; Chadwick, N.; Obaid, A. Y.; Al-Thabaiti, S.; Basahel, S. N.; Carmalt, C. J.; Parkin, I. P., Aerosol assisted chemical vapor deposition of conductive and photocatalytically active tantalum doped titanium dioxide films. *Journal of Materials Chemistry A* **2014,** *2* (32), 12849-12856.

16. Regonini, D.; Groff, A.; Sorarù, G.; Clemens, F., Suppressing deep traps in self-organized TiO2 nanotubes by nb doping and optimized water content. *Journal of the Electrochemical Society* **2016,** *163* (3), H243.
17. Yan, Y.; Lee, J.; Cui, X., Enhanced photoelectrochemical properties of Ta-TiO2 nanotube arrays prepared by magnetron sputtering. *Vacuum* **2017,** *138*, 30-38.
18. Hsu, C.-H.; Chen, K.-T.; Lin, L.-Y.; Wu, W.-Y.; Liang, L.-S.; Gao, P.; Qiu, Y.; Zhang, X.-Y.; Huang, P.-H.; Lien, S.-Y., Tantalum-Doped TiO2 Prepared by Atomic Layer Deposition and Its Application in Perovskite Solar Cells. *Nanomaterials* **2021,** *11* (6), 1504.
19. Zhang, H.; Li, D.; Byun, W. J.; Wang, X.; Shin, T. J.; Jeong, H. Y.; Han, H.; Li, C.; Lee, J. S., Gradient tantalum-doped hematite homojunction photoanode improves both photocurrents and turn-on voltage for solar water splitting. *Nature communications* **2020,** *11* (1), 4622.
20. Wang, Y.; Tan, Q.; Huang, B., Synthesis and properties of novel N/Ta-co-doped TiO2 coating on titanium in simulated PEMFC environment. *Journal of Alloys and Compounds* **2021,** *879*, 160470.
21. Liu, X.; Wu, X.; Scott, K., Study of niobium and tantalum doped titania-supported Pt electrocatalysts for methanol oxidation and oxygen reduction reactions. *Catalysis Science & Technology* **2014,** *4* (11), 3891-3898.
22. Usui, H.; Domi, Y.; Takama, K.; Tanaka, Y.; Sakaguchi, H., Tantalum-doped titanium oxide with rutile structure as a novel anode material for sodium-ion battery. *ACS Applied Energy Materials* **2019,** *2* (5), 3056-3060.
23. Kresse, G.; Furthmüller, J., Efficiency of ab-initio total energy calculations for metals and semiconductors using a plane-wave basis set. *Computational materials science* **1996,** *6* (1), 15-50.
24. Kresse, G.; Furthmüller, J., Efficient iterative schemes for ab initio total-energy calculations using a plane-wave basis set. *Physical review B* **1996,** *54* (16), 11169.
25. Blöchl, P. E., Projector augmented-wave method. *Physical review B* **1994,** *50* (24), 17953.
26. Perdew, J. P.; Burke, K.; Ernzerhof, M., Generalized gradient approximation made simple. *Physical review letters* **1996,** *77* (18), 3865.
27. Monkhorst, H. J.; Pack, J. D., Special points for Brillouin-zone integrations. *Physical review B* **1976,** *13* (12), 5188.
28. Anisimov, V. I.; Zaanen, J.; Andersen, O. K., Band theory and Mott insulators: Hubbard U instead of Stoner I. *Physical Review B* **1991,** *44* (3), 943.
29. Morgan, B. J.; Watson, G. W., A DFT+ U description of oxygen vacancies at the TiO2 rutile (1 1 0) surface. *Surface Science* **2007,** *601* (21), 5034-5041.
30. Calzado, C. J.; Hernández, N. C.; Sanz, J. F., Effect of on-site Coulomb repulsion term U on the band-gap states of the reduced rutile (110) Ti O 2 surface. *Physical Review B* **2008,** *77* (4), 045118.
31. Kumaravel, V.; Rhatigan, S.; Mathew, S.; Bartlett, J.; Nolan, M.; Hinder, S. J.; Sharma, P. K.; Singh, A.; Byrne, J. A.; Harrison, J., Indium Doped TiO2 Photocatalysts with High Temperature Anatase Stability. *The Journal of Physical Chemistry C* **2019,** *123*, 21083-21096.
32. Kumaravel, V.; Rhatigan, S.; Mathew, S.; Michel, M. C.; Bartlett, J.; Nolan, M.; Hinder, S. J.; Gascó, A.; Ruiz-Palomar, C.; Hermosilla, D., Mo doped TiO2: impact on oxygen vacancies, anatase phase stability and photocatalytic activity. *Journal of Physics: Materials* **2020,** *3* (2), 025008.
33. Henkelman, G.; Arnaldsson, A.; Jónsson, H., A fast and robust algorithm for Bader decomposition of charge density. *Computational Materials Science* **2006,** *36* (3), 354-360.
34. Nagaraju, G.; Karthik, K.; Shashank, M., Ultrasound-assisted Ta2O5 nanoparticles and their photocatalytic and biological applications. *Microchemical Journal* **2019,** *147*, 749-754.

35. Singh, N.; Prakash, J.; Misra, M.; Sharma, A.; Gupta, R. K., Dual functional Ta-doped electrospun TiO2 nanofibers with enhanced photocatalysis and SERS detection for organic compounds. *ACS applied materials & interfaces* **2017,** *9* (34), 28495-28507.
36. Shang, B.; Liang, P.; Li, F.; Chao, X.; Wei, L.; Yang, Z., Dielectric response of TiO2 ceramics: The crucial role of Ta2O5. *Journal of Alloys and Compounds* **2017,** *704*, 64-69.
37. Tuichai, W.; Thongyong, N.; Danwittayakul, S.; Chanlek, N.; Srepusharawoot, P.; Thongbai, P.; Maensiri, S., Very low dielectric loss and giant dielectric response with excellent temperature stability of Ga3+ and Ta5+ co-doped rutile-TiO2 ceramics. *Materials & Design* **2017,** *123*, 15-23.
38. Baiju, K.; Shajesh, P.; Wunderlich, W.; Mukundan, P.; Kumar, S. R.; Warrier, K., Effect of tantalum addition on anatase phase stability and photoactivity of aqueous sol–gel derived mesoporous titania. *Journal of Molecular Catalysis A: Chemical* **2007,** *276* (1-2), 41-46.
39. Ranjan, R.; Prakash, A.; Singh, A.; Singh, A.; Garg, A.; Gupta, R. K., Effect of tantalum doping in a TiO 2 compact layer on the performance of planar spiro-OMeTAD free perovskite solar cells. *Journal of Materials Chemistry A* **2018,** *6* (3), 1037-1047.
40. Gong, Y.; Fu, C.; Ting, L.; Chenu, J.; Zhao, Q.; Li, C., Exploring the effect of boron and tantalum codoping on the enhanced photocatalytic activity of TiO2. *Applied Surface Science* **2015,** *351*, 746-752.
41. Krishnaprasanth, A.; Seetha, M., Solvent free synthesis of Ta2O5 nanoparticles and their photocatalytic properties. *AIP advances* **2018,** *8* (5), 055017.
42. Sheppard, L. R.; Hager, S.; Holik, J.; Liu, R.; Macartney, S.; Wuhrer, R., Tantalum segregation in Ta-Doped TiO2 and the related impact on charge separation during illumination. *The Journal of Physical Chemistry C* **2015,** *119* (1), 392-400.